PAPER REF: 3863

THE INFLUENCE OF CONTOURING ON THE TENSILE STRENGTH OF FUSED DEPOSITION MODELLING PROCESSED PARTS

Dario Croccolo[1(*)], Massimiliano De Agostinis[1], Giorgio Olmi[1]

[1]Department of Industrial Engineering (DIN), University of Bologna, Bologna, Italy
[(*)]*Email:* dario.croccolo@unibo.it

ABSTRACT

The Fused Deposition Modelling process is a highly efficient Rapid Prototyping approach that makes it possible to rapidly generate even much complicated parts. Unfortunately, the Fused Deposition Modelling is affected by several parameters, whose setting may have a strong impact on the components resistance. This paper is dedicated to the study of the effects generated by the Fused Deposition Modelling production parameters on the tensile strength and on the stiffness of the generated components, tackling the question both from experimental and from numerical points of view. For this purpose, an analytical model was developed, which is able to predict the resistance and the stiffness properties, based on the number of contours deposited around the component edge and on the setting of the other main parameters of the deposition process.

Keywords: Fused Deposition Modelling (FDM), Strength, Stiffness, Contouring, Analytical model

INTRODUCTION

The Rapid Prototyping (*RP*) process experienced great advances in the last years: nowadays, it is possible to build parts, having even very complicated geometries in a short time and at low costs when their requested mechanical proprieties are not too high. The main advantages consist in the easy generation of a 3D prototype from a concept and in the possibility of making the manufacturing and assembly tasks less complicated. For this purpose, it is often possible to consolidate sub assemblies into single units, thus reducing the number of parts, the handing time, and the number of mating surfaces, which helps simplifying the mounting task. Moreover, the *RP* process is highly flexible since it is easy and economic to rearrange the process, when design changes must be taken into account. Unfortunately the strength and stiffness of components realised with this technology are not so much high and they are difficult to be defined also because they have a strong anisotropy.

The Fused Deposition Modeling (*FDM*) from Stratasys is a typical example of a *RP* process, leading to the aforementioned characteristics. The *FDM* is able to produce prototypes from plastic materials, such as *ABS* or *ULTEM*, and the process consists in the deposition of filaments of the material at the semi-molten state. The filament is fed through a nozzle, located at the output of a heating device, and is deposited onto the partially constructed part. Since the material is extruded and laid in tracks at a semi-molten state, the newly deposited material fuses with adjacent material that has already been deposited. Afterwards, other material tracks are deposited, upon the completion of the current layer; then the deposition of a new layer is started.

The final mechanical properties of parts obtained by means of the FDM process, are, often, uncertain since they are influenced by a large combination of production parameters, which

are, really, difficult to combine in order to increase the strength and the stiffness of the realised parts. As a consequence, the practical application of components processed by the *FDM* (and in general by *RP* techniques), is limited to low loaded products and to those whose failures do not lead to severe effects. Regarding this issue, Refs. (Lee, 2005; Howell, 2001) contain the remark that *FDM* processed parts may have some potentials for use in fields of mechanics, where compliant members or mechanisms are used. Possible applications are in the manufacturing of electro-mechanical actuators or in that of children's toys, for instance bows and arrows or small catapults as presented by (Lee, 2005). In these cases, the not high resistance is well compensated by the lower cost, by an easier mounting process and especially by good elastic properties. It is therefore important to predict not only the strength, but also the stiffness, and how they relate to process parameters.

The main factors, potentially having an impact on the product properties, are the part building direction (inclination of part in a build platform, as it is being generated), the bead width, the raster angle (direction of the beads), the air gap (gap between two adjacent rasters on the same layer) and the layer thickness (thickness of the deposited layer).

Several papers deal with the influence of these parameters: the issue is mainly tackled by running experimental campaigns, assisted by techniques of Design of Experiment (*DOE*). The experimental task presented in (Ahn, 2002) involved flat specimens tested under axial load, in agreement with the Standard for tensile tests on plastics. The results emphasize the effect of the raster orientation and of the air gap, while the bead width does not seem to have a great effect. The resistance is magnified, as the direction of the beads is parallel to that of load, while is very low when the rasters are perpendicular to the applied force. The air gap has an easily comprehensible effect: when it is positive, the structure is loosely packed, can be rapidly generated, but has a lower strength, conversely a negative air gap increases the building time, but also the density and, consequently, the strength of products. The influence of these parameters is confirmed also in (Lee, 2005), with reference to *FDM* processed sling shot toys. Anitha (2001) also studied the effect of the layer thickness, which proved to increase the performance when the thickness decreases. On the other hand, the raster width confirms to be of a low significance. The *FDM* processed parts exhibit anisotropic properties not only regarding the raster orientation, but also with reference to the build orientation. The related effect is shown in (Lee, 2007) with reference to differently manufactured specimens to be loaded under compression. The choice of the plane on which the part is sitting during its generation has strong effects both on the cost and on the time of the process, as discussed in (Xu, 1999; Thrimurthulu, 2004). The previously cited parameters are considered in (Sood, 2010), where the authors perform an extensive experimentation on specimens under axial and flexural loads. Techniques of *DOE* are applied for the campaign planning and for the processing of the results. The surface response approach is successfully used for the development of analytical models relating the tensile strength to the levels of the process inputs.

What can be remarked is that no paper in literature deals with the effect of contouring. The conventional procedure of *FDM* requires the application of a sufficient number of offset contours around the edge of the modelled part; the internal part is filled by oriented rasters in order to fulfil the surface roughness requirements. Contouring not only affects the surface finishing, but also the tensile strength of components, and its effect may be even very strong, depending on the contour width and on its direction with respect to the load. Only in (Ahn, 2002) the contouring effect on the tensile strength is briefly tackled, emphasizing the important role at preventing stress concentration and crack initiation at the fillets, thus at improving the mechanical properties. However, no quantitative results are presented

regarding the relationship between the strength or the stiffness and the number of contours. Another interesting aspect regards *predictive models*, i.e. models that, taking the aforementioned factors into account, are able to predict the part resistance. As previously remarked an interesting empirical model was developed in (Sood, 2010), but it also does not take the contouring effect into account, moreover the part stiffness is not investigated.

The present paper investigates the effect of contouring by running suitable experimental tests, and by developing an analytical model that is able to match the experimental results. The analytical model is useful to get a better comprehension of the structural response of *FDM* processed parts and to predict their behaviour in terms of strength and stiffness, based on the parameters of the process.

MATERIALS AND METHODS

The experimental campaign involved specimens made of *ABS-M30*, a widely used material for *FDM* processed parts. Its mechanical properties are the following: Ultimate Strength of a single bead, US_b=33MPa, Elastic Modulus of a single bead, E_b=2,400MPa, Tensile Elongation to failure EF=4%. The material characterization was performed on samples manufactured by injection moulding supplied by the material producer. Injection moulded specimens are commonly used (Ahn, 2002) with the purpose of determining reference values for strength and stiffness of plastic materials (such as *ABS*) in isotropic conditions.

The first step in the arrangement of the experimental campaign consisted in the design of specimens and in the determination of the related parameters. The specimens have been shaped according to the *ASTM D638 – 10 (ASTM D638, 2010)* Standard, with reference to the geometry of the first typology. A drawing of the specimen (a flat dog bone shaped specimen with uniform rectangular section at the gage and head connected with large fillets) is shown in Fig. 1 with the indication of its main dimensions. The curvature radius has been carefully chosen at a preliminary stage of the research: specimens with the same geometry but different fillet radii have been manufactured and tested under tensile load. By examining the fracture locations, the most suitable radius value has been determined, in order to significantly reduce the stress concentration at the fillet, thus to avoid the crack initiation. A radius of 244mm, much greater than that suggested by the aforementioned Standard, was finally chosen as the best compromise between the specimen full length and the necessity to prevent unacceptable ruptures at the fillet; this is an important issue, since this kind of failures could have been enhanced by the anisotropic structure of the material (Ahn, 2002).

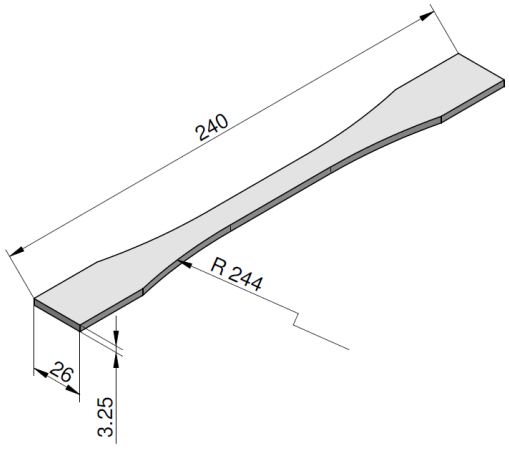

Fig.1 Specimen geometry with its main dimensions in mm.

Five different types of specimen have been manufactured by varying the two following parameters:

- The building orientation: specimens grown up along the thickness or along one of the two principal dimensions.
- The number of contour lines: number of contours deposited close to the edges of components along one of the two principal dimensions.

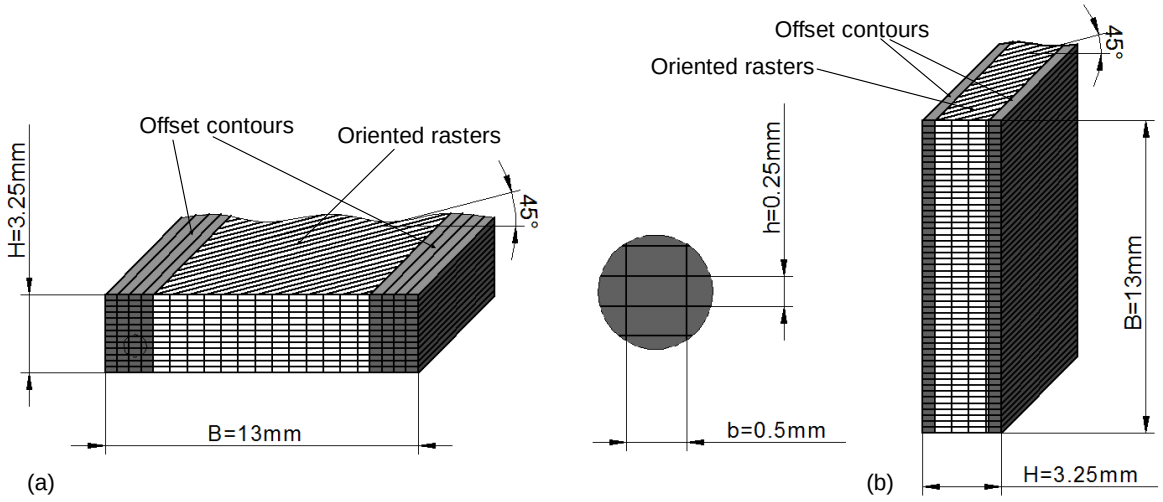

Fig.2 Generation of specimen types: (a) type 2 and (b) type 5, with details on geometry and main dimensions

The combination of the aforementioned parameters, which generates the different layout of contour planes, is well clarified in Fig. 2. The *offset contours* (coloured in grey) are, firstly, deposited in a stated number around the specimen edges. In Fig. 2 (a) is represented a *4 contoured* specimen with the *along the thickness* building orientation whereas in Fig. 2 (b) is represented a *1 contoured* specimen with the *along one of the principal dimension* building orientation; thus the total number of deposition planes depends on the building orientation Then the *FDM* machine deposits alternate layers by changing the direction of the beads usually from +45° to -45° in order to fill in the empty space left by the contours deposition. Four sample types have been generated with the *along the thickness* building orientation such as the example of Fig. 2 (a): they have, respectively, 1 (Type 1), 4 (Type 2), 7 (Type 3) and 10 (Type 4) contours. The Type 5 specimen generated with the *along one of the principal dimension* building orientation such as the example of Fig. 2 (b), has 1 contour line. The other factors have been kept at fixed levels: the bead width, which proved to be of a poor significance (Ahn, 2002), has been maintained at the value of 0.5mm while the raster angle has been set as +45°/-45°. This is the mostly used setting, resulting in a pattern of beads, all having the same inclinations with respect to the specimen axis, and also to the load direction. The air gap has been kept at the value of 0mm (meaning that the beads are all adjacent to each other). The effect of this factor is well clarified by (Lee, 2005), moreover a 0mm air gap is the generally used setting, as a positive value leads to parts with bad surface finishing, whereas the negative values lead to dense components, with too long manufacturing times for *RP* applications. Finally, the layer thickness has been set to 0.25mm, which is again the most widely used value (one half of the bead width), considered also in (Sood, 2010; Lee, 2007). The specimen features are summarized in Table 1.

Table 1 Factors and related levels

Factor	Level
Building orientation and number of contour lines	Specimen built *along the thickness* with 1, 4, 7, 10 contour lines (Types 1, 2, 3, 4). Specimen built *along one of the principal dimension* with 1 contour line (Type 5)
Bead width	0.5 mm (dimension *b* in Fig. 2)
Raster angle	+45°/-45°
Air gap	0mm
Layer thickness	0.25mm (dimension *h* in Fig. 2)

Five samples have been considered for each specimen type, following the recommendations of *ASTM D638, 2010* Standard and of most Standards dealing with static tests on plastics.

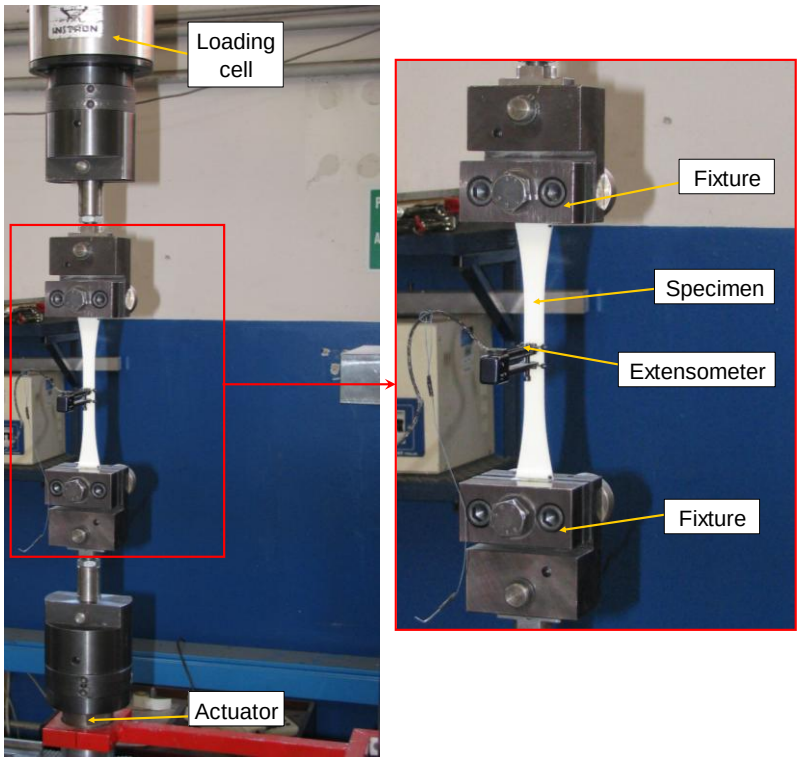

Fig.3 Experimental set-up during a tensile test

The tests have been performed on an oleo-dynamic press in the displacement-controlled mode at the actuator velocity of 20μm/s. Since misalignments may seriously affect the results (Olmi, 2011), each specimen has been carefully aligned with respect to load and fully constrained at machine clamps: for this purpose, the length of the specimen heads was

suitably chosen, depending on the length of the fixtures. Afterwards, an extensometer with a maximum elongation of 5mm and a knife-edge distance of 12.5mm, has been applied at specimen gage for the on-line measurement (open loop measurement) of longitudinal strain, thus meeting the requirements of *ASTM D638, 2010* Standard. A photo of the experimental set-up is shown in Fig. 3. The considered outputs are three: the gage strain by the extensometer, the entity of load and the actuator displacement throughout the whole test. These two yields were provided directly by the testing machine, in particular load has been measured by a loading cell having a full scale of 25kN, which appeared to be adequate, if compared to that used in (Ahn, 2002). The measuring chain consisted of the three aforementioned analog outputs, connected to a connector block. The platform output was connected to a *DAQ Card*, inserted into a laptop slot. A specifically developed *LabView* program assisted the data acquisition task: sampling was conducted at the 20Hz rate, with on-line data recording during the test and automatic detection of the maximum load. The experimental results have been processed for the determination of the stress-strain curves, of the slopes in the linear field, namely the Young's modulus (*E*), and of the strengths in terms of the maximum load before failure (*US*).

EXPERIMENTAL RESULTS

Some examples of the stress-strain curves determined experimentally are shown in Fig. 4 (a) for the specimen types 1 to 4, i.e. specimens generated *along the thickness*, with different numbers of contours. By comparing the curves, it can be observed that the greater is the number of contours, the greater is the stiffness (as well as the elastic modulus) and the greater is the maximum strength. Moreover, when the number of contours increases, the percentage of elongation to failure decreases (with the exception of the first specimen type), indicating a more brittle behaviour.

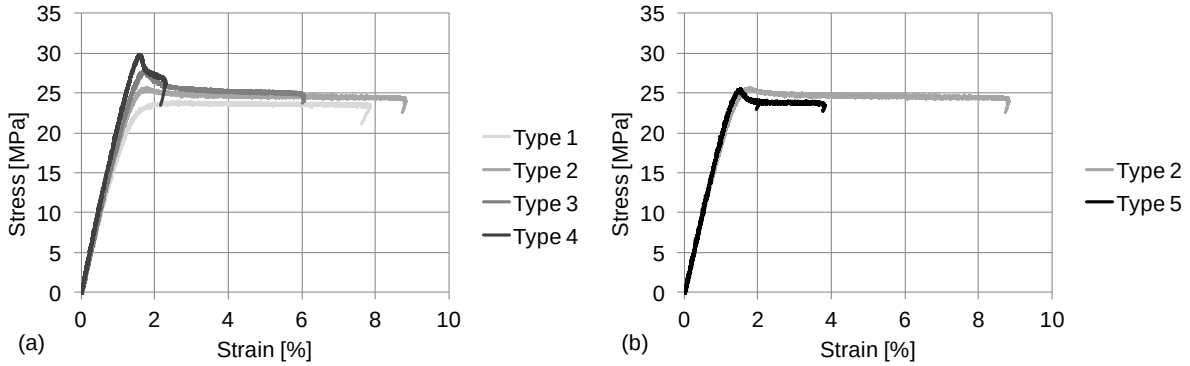

Fig.4 Stress-Strain curves obtained for specimens of different types

Samples of stress-strain curves for specimen types 5 and 2 are compared in Fig. 4 (b). It can be observed that they are very close: a possible reason is that these two specimen types have the same overall number of offset contours, considering the number of contours per layer multiplied by the total number of layers, Eq. (1).

$$N_c = 2n_c \cdot n_l \tag{1}$$

In Eq. (1) the terms n_c and N_c indicate the number of contours per layer and the overall number of contours respectively, while the symbol n_l stands for the number of layers. Eq. (1) results in Eqs. (2) and (3) accounting for specimen types 2 and 5, where subscripts are related to the two types. As reported in Table 1, the symbol *h* stands for the layer thickness.

$$N_{c2} = 2 \cdot 4 \cdot \frac{H}{h} \tag{2}$$

$$N_{c5} = 2 \cdot 1 \cdot \frac{B}{h} \tag{3}$$

It can be easily observed that $N_{c2}=N_{c5}$.

All the results have been processed for the determination of strengths and of Young's moduli. Following the recommendations of *ASTM D638, 2010* Standard, the Ultimate Strength (*US)* has been computed as a ratio between the maximum load in the test and the full cross-sectional area at specimen gage. The calculation of *US* is shown in Eq. (4), where $F_{max.}$ indicates the maximum force value throughout the test, while *B* and *H* are the two dimensions of the rectangular cross-section at specimen gage.

$$US = \frac{F_{\max.}}{B \cdot H} \tag{4}$$

The Young's modulus (*E*) has been determined, considering the first linear portion of the stress-strain curve and estimating its slope by linear fitting procedures. The obtained values are shown in the two histograms in Fig. 5: they are estimated as averages over five replications. The worst scenario of twice the standard deviation is here considered for the determination of confidence intervals.

Again the results for Type 5 specimens appear to be quite close to those computed for Type 2 specimens.

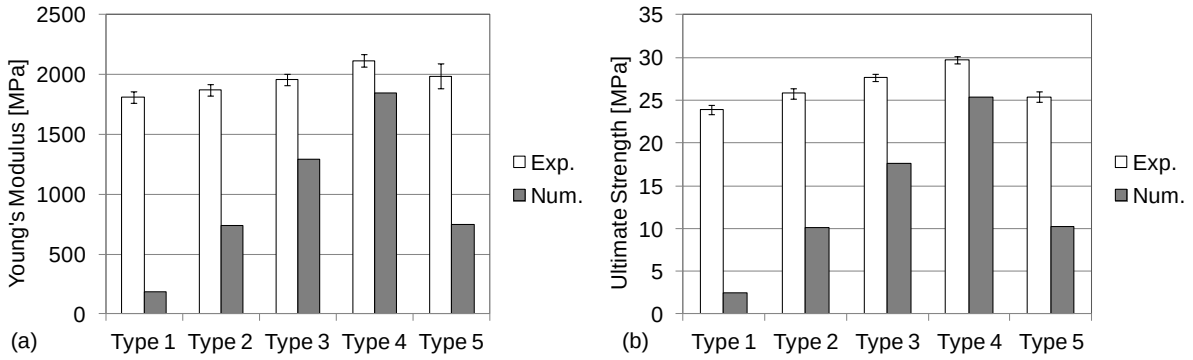

Fig.5 Comparison between the experimental data (Young's Modulus and Ultimate Strength) and the results of a rough numerical model considering the longitudinal beads only

The obtained results seem to suggest that the mechanical response of the tested specimens is strictly related to the total number of contours, i.e. beads having a longitudinal layout; when

the number of contour lines is the same, whatever is the manufacturing procedure, the specimens have the same mechanical behaviour. Moreover, when the total number of contours increases, both the stiffness and the strength increase. In the current hypothesis (just the longitudinal beads drive the specimen response) the Ultimate Strength computed analytically (US_{ac}) and the Young's modulus (E_{ac}) can be computed as follows.

$$US_{ac} = \frac{US_b \cdot b \cdot h \cdot N_c}{B \cdot H} \tag{5}$$

$$E_{ac} = \frac{E \cdot b \cdot h \cdot N_c}{B \cdot H} \tag{6}$$

In the histograms of Fig. 5, the values computed by Eqs. (5) and (6) are compared to those experimentally retrieved. The serious disagreement observed indicates that the mechanical properties must depend on the inclined beads so that they have to be, actually, considered in the model.

This consideration is well supported by the maximum discrepancies observed in the case of Type 1 specimens, where almost the totality of the cross section consists of oriented rasters. Therefore, there is indeed a strict relationship between the number of contours and the mechanical response, however this simple relationship is not sufficient to fully understand and predict the mechanical behaviour. This was the main motivation to the development of the following analysis that considers both longitudinal and oriented rasters co-operating to sustain the applied load.

ANALYTICAL MODEL

The analytical model has been developed according to some hypotheses, summarized in the following lines.

- According to *ASTM D638, 2010* Standard, *FDM* specimens can be regarded as slender beams, whose length is much greater than width and height. Consequently, it appears to be reasonable to presume an infinite length of the specimen gage. As the external load is applied, the specimen gage gets deformed with uniformly distributed strain.
- The infinite gage is meshed into a series of elements, whose characteristics are suitably defined for each specimen type, as detailed below.
- In each of these elements the total load is shared between longitudinal and inclined rasters, so that their axial elongation is maintained the same. In other words, all the beads co-operate to sustain the total load, working in parallel.

The model is able to process the following inputs.

- Geometry data regarding the overall dimensions of the section (*B* and *H*), the bead width and height (*b* and *h*) and the raster angle for alternate layers ($\pm\alpha$).
- The elongation under axial load of a portion of the specimen gage considered as an "element", whose length must be suitably determined as exposed below. The entity of this elongation is called *v*.

- The ultimate strength US_b of each bead.

The outputs are finally the following data.

- Estimation of the current axial force applied to the specimen, with reference to its elongation.
- Determination of specimen stiffness, as well as its Young's modulus.
- Estimation of the tensile strength, by a suitable modelling of the breakage event, as a consequence of failures of longitudinal and angled beads.

It must be remarked that, since the elements are connected in series, they transmit the same external load. Consequently, it is sufficient to compute the load transmitted by one element, to determine the current load being axially applied to the whole specimen.

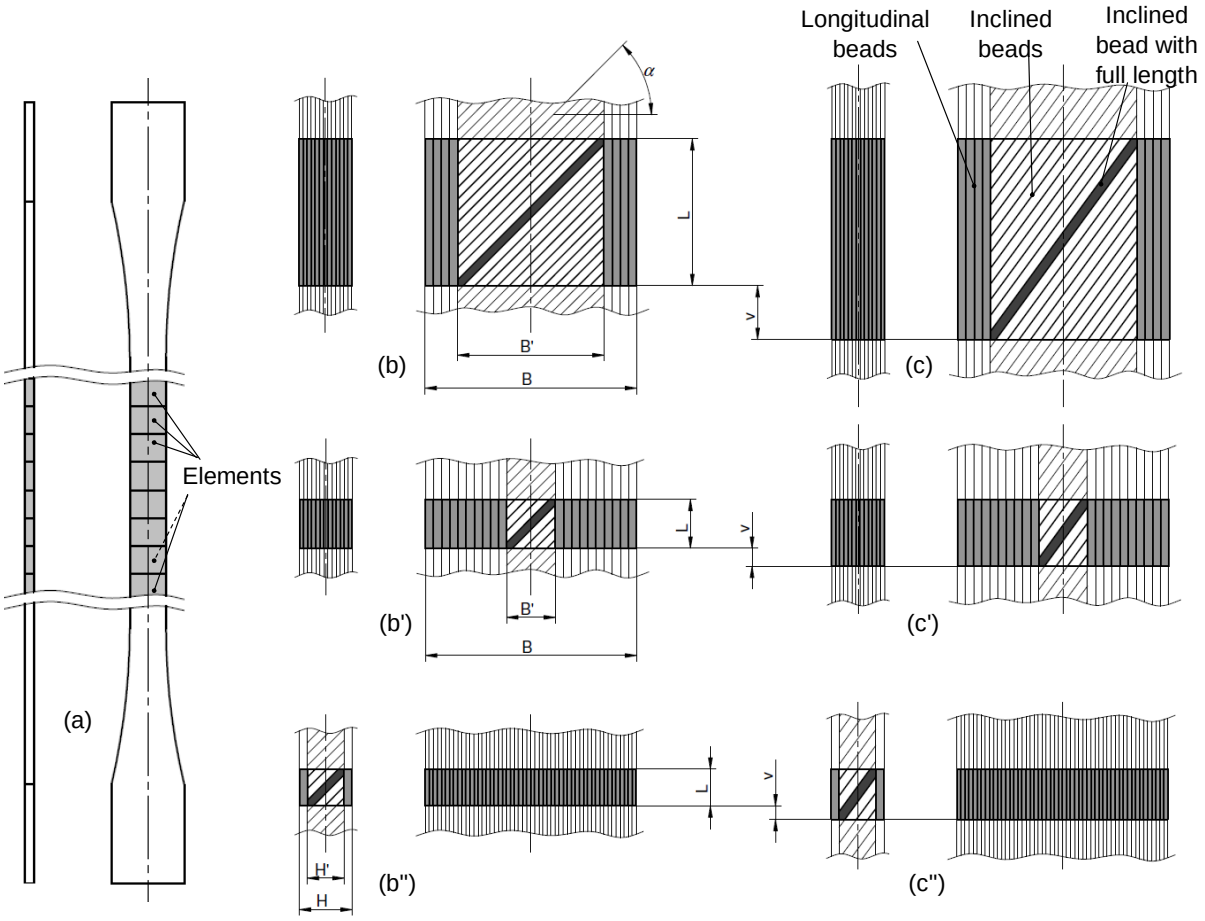

Fig.6 Side and front views of the specimen gages meshed into several elements: (a) the whole gauge, (b), (b'), (b") undeformed and enlarged view, (c), (c'), (c") deformed and enlarged view for specimen types 2 (b, c), 4 (b', c'), 5 (b", c")

Some samples of elements for specimen Types 2, 4 and 5 are shown in Fig. 6. It can be observed that their length is adjusted, so that each element, independently of the specimen type, contains the same typologies of beads, in particular (referring to one layer):

- Longitudinal rasters.

- One inclined bead, extended over the width *B'* or *H'*.
- Some shorter and inclined beads symmetrically disposed with respect to the inclined bead extended over the width *B'* or *H'*.

Each element covers the whole cross section and has a length depending on the number of contours, on the specimen type and on the inclination angle. In particular, the element length is computed by Eq. (7) for Types 1 to 4 and by Eq. (8) for Type 5, where the terms *B'* and *H'* stand for the width of the section containing inclined beads.

$$L = \left(B - 2n_c \cdot b\right) \cdot tg\left(\alpha\right) = B' \cdot tg\left(\alpha\right) \tag{7}$$

$$L = \left(H - 2n_c \cdot b\right) \cdot tg\left(\alpha\right) = H' \cdot tg\left(\alpha\right) \tag{8}$$

As shown in the sketch of Fig. 6 the dilatation of a single element is indicated by the *v* parameter. The current load transmitted by the rasters can be determined once the displacement *v* and the stiffness properties of the beads are known: full details on the computation procedures are provided in the following paragraph.

Longitudinal rasters

The stiffness of each longitudinal bead (k_l) can be easily estimated, according to Eq. (9), where the single bead is modelled as a longitudinal beam loaded by an axial force. The force transmitted by each bead is computed as the product between the stiffness and the applied displacement *v*. Since all the rasters work as a parallel of springs, the total value of the axial force (F_l) transmitted by the contours of a single layer is given by Eq. (10), where the force transmitted by one bead is multiplied by the number of longitudinal rasters.

$$k_l = \frac{Ebh}{L} \tag{9}$$

$$F_l = k_l \cdot v \cdot 2 \cdot n_c \tag{10}$$

Inclined bead with full length

The model of the inclined bead is represented in the scheme of Fig. 7, where a slender beam is loaded by a vertical force, along the specimen axis. When the force is applied, an axial load is transmitted to the beam so that the inclined bead gets axially deformed. Its deformation implies a vertical displacement *v* of its lower extremity. As previously remarked, the entity of the displacement *v* is the driving factor of the analytical model. The intensity of the vertical force, $F_{\alpha(0)}$, transmitted by the inclined bead may be determined as a function of *v*, by means of the procedure described below.

Let $l_{(0)}$ and $\Delta l_{(0)}$ be respectively the length of the inclined bead and its elongation under the applied load. Considering the scheme reported in Fig. 7, the Eqs. (11) and (12) can be easily determined; the meaning of angle γ is clarified in the same figure.

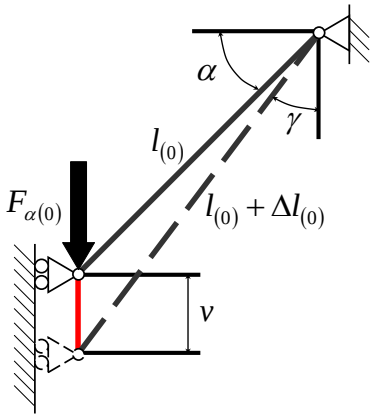

Fig.7 Model of the inclined bead loaded by the force $F_{\alpha(0)}$ and elongated with vertical displacement v

$$\left(l_{(0)} + \Delta l_{(0)}\right)\sin(\gamma) = l_{(0)}\cos(\alpha) \tag{11}$$

$$\left(l_{(0)} + \Delta l_{(0)}\right)\cos(\gamma) = v + l_{(0)}\sin(\alpha) \tag{12}$$

The entity of displacement v can be computed by solving Eq. (12), while the relationship in Eq. (11) can be used to determine the sine of the angle γ. Thus in Eq. (13) v can be expressed as a function of geometrical parameters.

$$\begin{aligned} v &= \left(l_{(0)} + \Delta l_{(0)}\right)\cos(\gamma) - l_{(0)}\sin(\alpha) = \left(l_{(0)} + \Delta l_{(0)}\right)\sqrt{1-\sin^2(\gamma)} - l_{(0)}\sin(\alpha) = \\ &= \sqrt{\left(l_{(0)} + \Delta l_{(0)}\right)^2 - {l_{(0)}}^2\cos^2(\alpha)} - l_{(0)}\sin(\alpha) = l_{(0)}\left[\sqrt{\left(1+\frac{\Delta l_{(0)}}{l_{(0)}}\right)^2 - \cos^2(\alpha)} - \sin(\alpha)\right] \end{aligned} \tag{13}$$

The following step consists in the determination of the relationship between $F_{\alpha(0)}$ and v. By considering again the scheme in Fig. 7, the axial load acting on the bead can be easily calculated as $F_{\alpha(0)}/\sin(\alpha)$. Thus, considering the stiffness of a beam under axial load the elongation $\Delta l_{(0)}$ is given by Eq. (14).

$$\Delta l_{(0)} = \frac{\dfrac{F_{\alpha(0)}}{\sin(\alpha)}}{\dfrac{E \cdot b \cdot h}{l_{(0)}}} = \frac{F_{\alpha(0)} l_{(0)}}{E \cdot b \cdot h \cdot \sin(\alpha)} \tag{14}$$

Then Eq. (14) joint with Eq. (13) results in Eq. (15) that can be regarded as an irrational equation in the unknown $F_{\alpha(0)}$. Finally $F_{\alpha(0)}$ can be easily determined by Eq. (16) as a function of a fixed displacement v, along the specimen axis.

$$v = l_{(0)}\left[\sqrt{\left(1+\frac{F_{\alpha(0)}}{E\cdot b\cdot h\cdot \sin(\alpha)}\right)^2-\cos^2(\alpha)}-\sin(\alpha)\right] \tag{15}$$

$$F_{\alpha(0)} = \left[\sqrt{\left(\frac{v}{l_{(0)}}+\sin(\alpha)\right)^2+\cos^2(\alpha)}-1\right]\cdot E\cdot b\cdot h\cdot \sin(\alpha) \tag{16}$$

Inclined beads with decreasing length

Each element exhibits a number of inclined beads with decreasing length proportional to the distance from the central raster (the full length one) considered in the previous paragraph. The scheme reported in Fig. 8 (a) shows the inclined beads in the element for a Type 2 specimen and their proportions with respect to the full length one indicated as the "bead (0)", while the others are referenced by increasing numbers. The total number of inclined beads, n_α, is given by Eq. (17) whereas the length of the (i-th) inclined bead, $l_{(i)}$, is expressed by Eq. (18).

$$n_\alpha = \frac{B_1}{b}\cdot \sin(\alpha) \tag{17}$$

$$l_{(i)} = \frac{B_1-\dfrac{i\cdot b}{\sin(\alpha)}}{B_1}\cdot l_{(0)} = \left[1-\frac{i\cdot b}{B_1\cdot \sin(\alpha)}\right]\cdot l_{(0)} = \frac{(n_\alpha - i)\cdot b}{B_1\cdot \sin(\alpha)}\cdot l_{(0)} \tag{18}$$

As explained in the previous paragraph, the vertical force, with direction along the specimen axis, must be computed as a function of the displacement v. In this case, the force sustained by the (i-th) inclined bead, $F_{\alpha(i)}$, must be determined. For this purpose, the procedure described in the previous paragraph can be used; however, the application of Eq. (16) requires a brief discussion.

Let us consider the (i-th) bead, having a $l_{(i)}$ length. By observing Fig. 8 (b) and with the hypothesis of all the beads working in parallel, it is clear that its lower extremity (i.e. point D) moves downwards by the displacement v. The entity of the total displacement v is given by the superposition of two effects: the elongation of the contour beads $v_{C(i)}$, which implies the vertical displacement of the upper extremity of the inclined bead (i.e. point C), and the elongation of the (i-th) bead itself $v_{(i)}$. Therefore the elongation v, as clearly indicated in Fig. 8 (b), results the sum of the two aforementioned contributions ($v=v_{C(i)}+v_{(i)}$). By inverting this relationship, the vertical displacement corresponding to the elongation of the (i-th) bead along its axis is $v_{(i)}=v-v_{C(i)}$ that is, of course, lower than the total displacement v. Therefore Eq. (16) is still valid for the computation of the force transmitted by the (i-th) bead, under the condition of replacing the displacement v by the term $v_{(i)}=v-v_{C(i)}$.

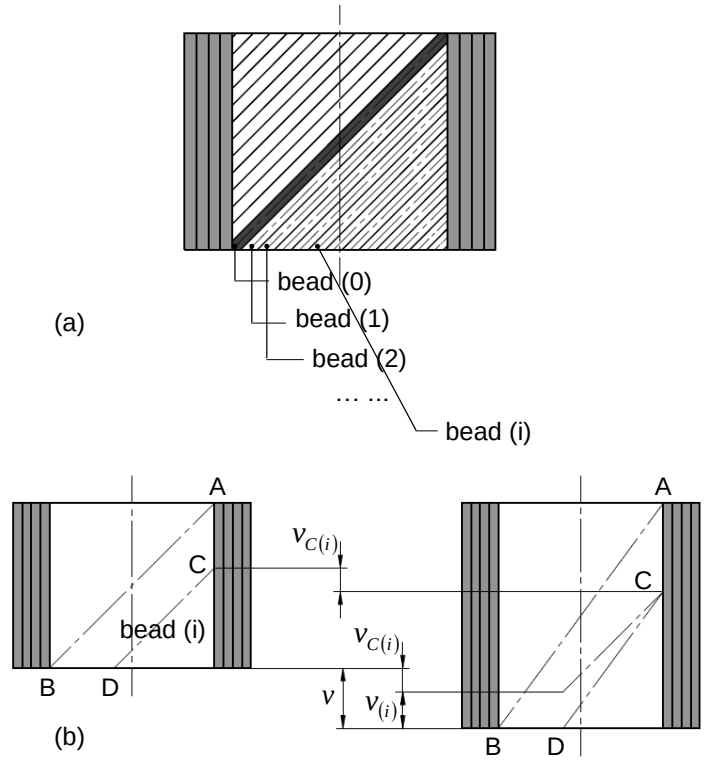

Fig.8 Inclined beads with reduced length (a) and determination of the vertical displacement to be considered in the stiffness model (b)

Under the hypothesis of uniform strain field at specimen gage, it is possible to easily compute $v_{C(i)}$, according to Eq. (19). The displacement $v_{(i)}$ is consequently computed as indicated in Eq. (20)

$$v_{C(i)} = \frac{v}{B_1 \cdot tg(\alpha)} \cdot \frac{i \cdot b}{\cos(\alpha)} = v \cdot \frac{i \cdot b}{B_1 \cdot \sin(\alpha)} \tag{19}$$

$$v_{(i)} = v - v_{C(i)} = v - v \cdot \frac{i \cdot b}{B_1 \cdot \sin(\alpha)} = \left(1 - \frac{i \cdot b}{B_1 \cdot \sin(\alpha)}\right) \cdot v = \frac{(n_\alpha - i) \cdot b}{B_1 \cdot \sin(\alpha)} \cdot v \tag{20}$$

It can be observed that the Eq. (20) is fully consistent with conditions at the boundaries, as the term $v_{(i)}$ is coincident with v for i=0, i.e. for the inclined bead with full length, and decreases to zero, for increasing value of i. For a great value of i the first effect $v_{C(i)}$, is much greater than the second one $v_{(i)}$: the axial dilatation of the inclined beads is in fact very low, due to reduced length and high axial stiffness. Since the ratio $v_{(i)}/l_{(i)}$ given by the ratio between Eq. (20) and Eq. (18) is equal to the ratio v/l, Eq. (16) is valid for all the inclined beads and results in Eq. (21).

$$F_{\alpha(i)} = \left[\sqrt{\left(\frac{v_{(i)}}{l_{(i)}} + \sin(\alpha) \right)^2 + \cos^2(\alpha)} - 1 \right] \cdot E \cdot b \cdot h \cdot \sin(\alpha) = F_{\alpha(0)} \tag{21}$$

Adhesive force between the beads

As previously remarked, in the *FDM* process an *ABS* filament is extruded through a nozzle and deposited onto the partially constructed part. As a consequence of a zero value of the air gap, all rasters are placed side by side. Thus, filament deposition at a semi-molten state implies that the just deposited track fuses with the adjacent material. The outcome is that any single bead is not completely free to get deformed under the applied load, as presumed above. Its elongation is partially constraint by the adhesive force acting at the interface between each couple of adjacent beads. Since the effect of the adhesive force arises from the difference between the elongations of the contiguous rasters, it is reasonable to apply the model represented in Eq. (22).

$$F_{ad.(i)} = 2 \cdot C_{ad.} \cdot \left| \Delta l_{(i)} - \Delta l_{(i-1)} \right| \tag{22}$$

The adhesive force at the interface between the (i-th) and the ((i-1)-th) beads, named, $F_{ad.(i)}$, is proportional to the difference between elongations ($\Delta l_{(i)}$ and $\Delta l_{(i-1)}$), with a constant, $C_{ad.}$, to be experimentally calibrated. Moreover, a factor two is considered to account for the effect of the adhesive forces between the inclined beads at the left-upper part of the element in Fig. 8 (a) symmetrically positioned respect to the inclined bead with full length. It can be observed that all the beads forming the longitudinal contours experience the same elongation, while the inclined rasters have generally different dilatations along their axes. Consequently, the adhesive force effect arises only when considering oriented rasters. This is the reason why the notations in Eq. (22) explicitly refer to this group of beads. Moreover, the greater is the number of inclined beads (e.g. for Type 1 specimen, see Fig. 6), the greater is the described effect.

Computation of the total vertical force and modelling the bead rupture event

In the previous paragraphs it has been shown how to determine the force transmitted by the longitudinal beads and the inclined rasters, over just one layer of the specimen section. The total force, yielded by the analytical model, F_a, is finally computed in Eq. (23), where the calculated components are combined together and the result is multiplied by the number of layers, n_l.

$$\begin{aligned} F_a &= n_l \cdot \left[F_l + F_{\alpha(0)} + F_{\alpha(1)} + \ldots + F_{\alpha(n_\alpha)} + F_{Ad.(1)} + \ldots + F_{Ad.(n_\alpha)} \right] = \\ &= n_l \cdot \left[F_l + (n_\alpha + 1) \cdot F_{\alpha(0)} + \sum_{i=1}^{n_\alpha} F_{Ad.(i)} \right] \end{aligned} \tag{23}$$

The whole algorithm has been implemented on a calc-sheet and completed by logical controls for the simulation of the failure event of every single bead. In particular, the computed force for each bead is compared to the maximum force along the sample axis that can be sustained by the rasters. It depends on the ultimate strength of a single bead, US_b, on the raster orientation (longitudinal or inclined), and on the raster angle. The threshold values for longitudinal and inclined beads, T_{a_l} and T_{a_α}, are respectively indicated in Eqs. (24) and (25).

$$T_{a\_l} = US_b \cdot b \cdot h \tag{24}$$

$$T_{a\_\alpha} = US_b \cdot b \cdot h \cdot \sin(\alpha) \tag{25}$$

The value of the force transmitted by the single bead is left unchanged, when lower than the related threshold, and is automatically switched to zero, when greater, thus modelling the local rupture event.

COMPARISON TO EXPERIMENTAL RESULTS AND DISCUSSION

The previously described model has been applied for the prediction of the mechanical behaviour of the tested samples, and then it has been compared with the experimental data for validation purposes.

Suitable stiffness models make it possible to compute the total force F_a, as a function of a fixed displacement v, related to the length of the gage element, i.e. dimension L of Fig. 6. The basic idea is to apply the analytical model as a simulation of an experimental tensile test. On one hand, trials have been conducted in displacement controlled conditions, with the force on-line measurement, on the other hand the numerical model has been applied in order to determine the F_a for a large amount of v values corresponding to the test runs from the start to specimen failure. Under the hypothesis of uniform strain over specimen gage, the strain value may be computed as v/L. The first step consists in the estimation of a sufficiently large strain range, from zero to the maximum elongation expected during the tensile tests. This range is assumed as the strain interval throughout the test to be simulated. The maximum strain value is then converted into a displacement value, by multiplying it by the length L of the element. This displacement interval is finally divided into a sufficiently high number of steps, thus reproducing the resolution of experimental sampling. Finally, every force value is divided by the gage cross section ($B \cdot H$) for the computation of nominal stress.

The preliminary step before the comparison between analytical and experimental results consisted in the calibration of the constant $C_{ad.}$ used in Eq. (22). For this purpose, the experimental results of the sample Type 1, have been taken into account. As mentioned above, the adhesive force effect involves the inclined beads, whereas it does not regard longitudinal contours. Accordingly the results related to Type 1 specimen has been considered for the calibration task since this geometry contains the largest number of inclined rasters with respect to all the investigated configurations. The value of $C_{ad.}$ parameter has been adjusted, so that the analytical results were able to match the experimental ones: reference was made to nominal stress values over a wide range of strain in the elastic field. The value of $C_{ad.}$=200N/mm has been determined and then maintained in the processing regarding the other sample types.

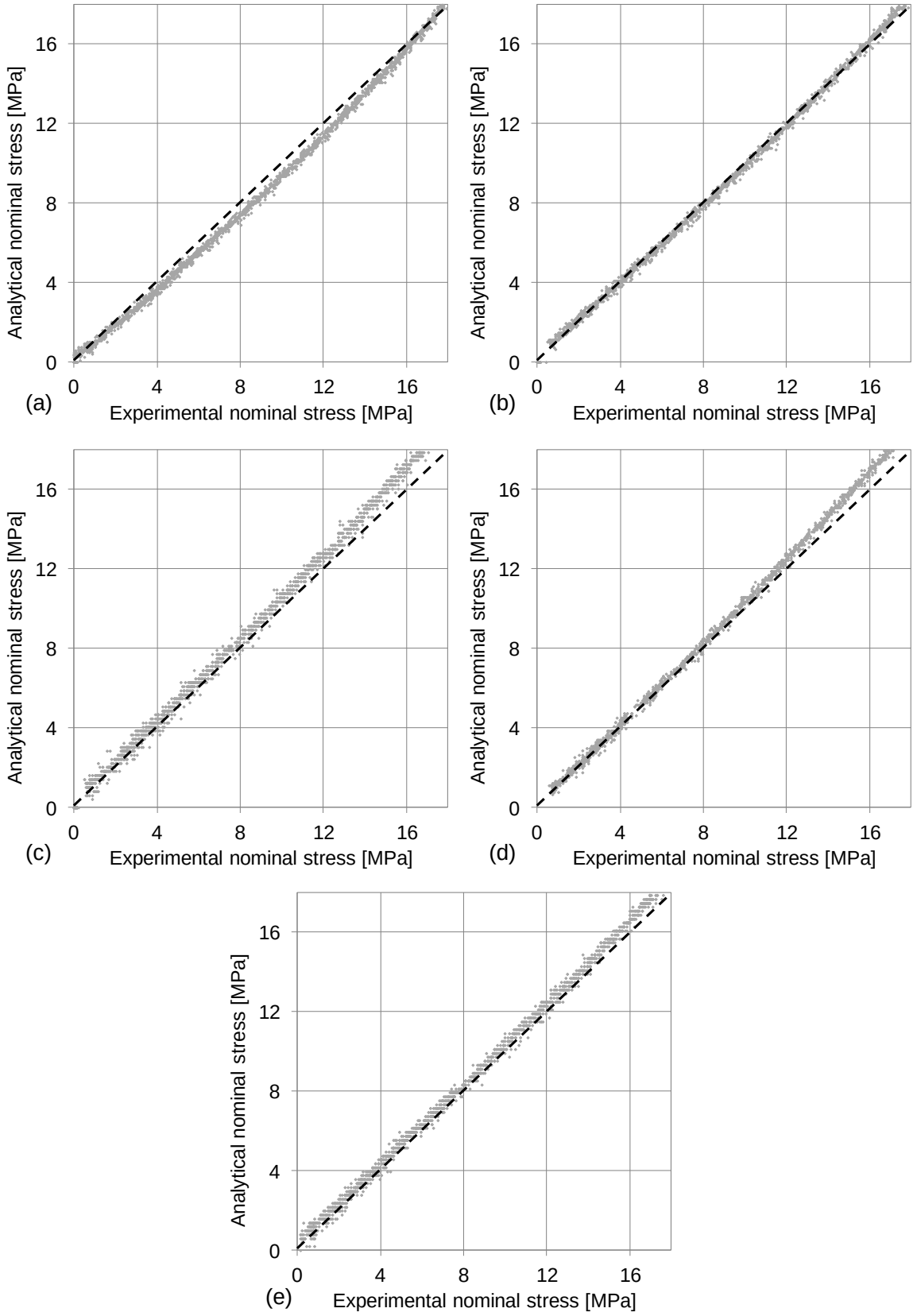

Fig.9 Analytical stresses plotted versus experimental ones for the same values of strains in the elastic field and for different specimen types: (a) Type 1, (b) Type 2, (c) Type 3, (d) Type 4, (e) Type 5

The diagrams reported in Fig. 9 show comparisons between the experimental values of nominal stress and the analytically computed ones. In particular, the analytical values are plotted versus the experimental ones, referring to the same strain at specimen gage in the linear-elastic field. The experimental data have been recorded during one of the five trials conducted for each specimen type. The previously mentioned calibration task has been performed, on the basis of the first diagram (Fig. 9 (a)), which refers to Type 1 specimen. By looking at the other diagrams (Fig. 9 (b-e)), a good agreement can be remarked: all the data points are very close to the diagonal line (representing perfect agreement) and the errors are in the order of few percentage points.

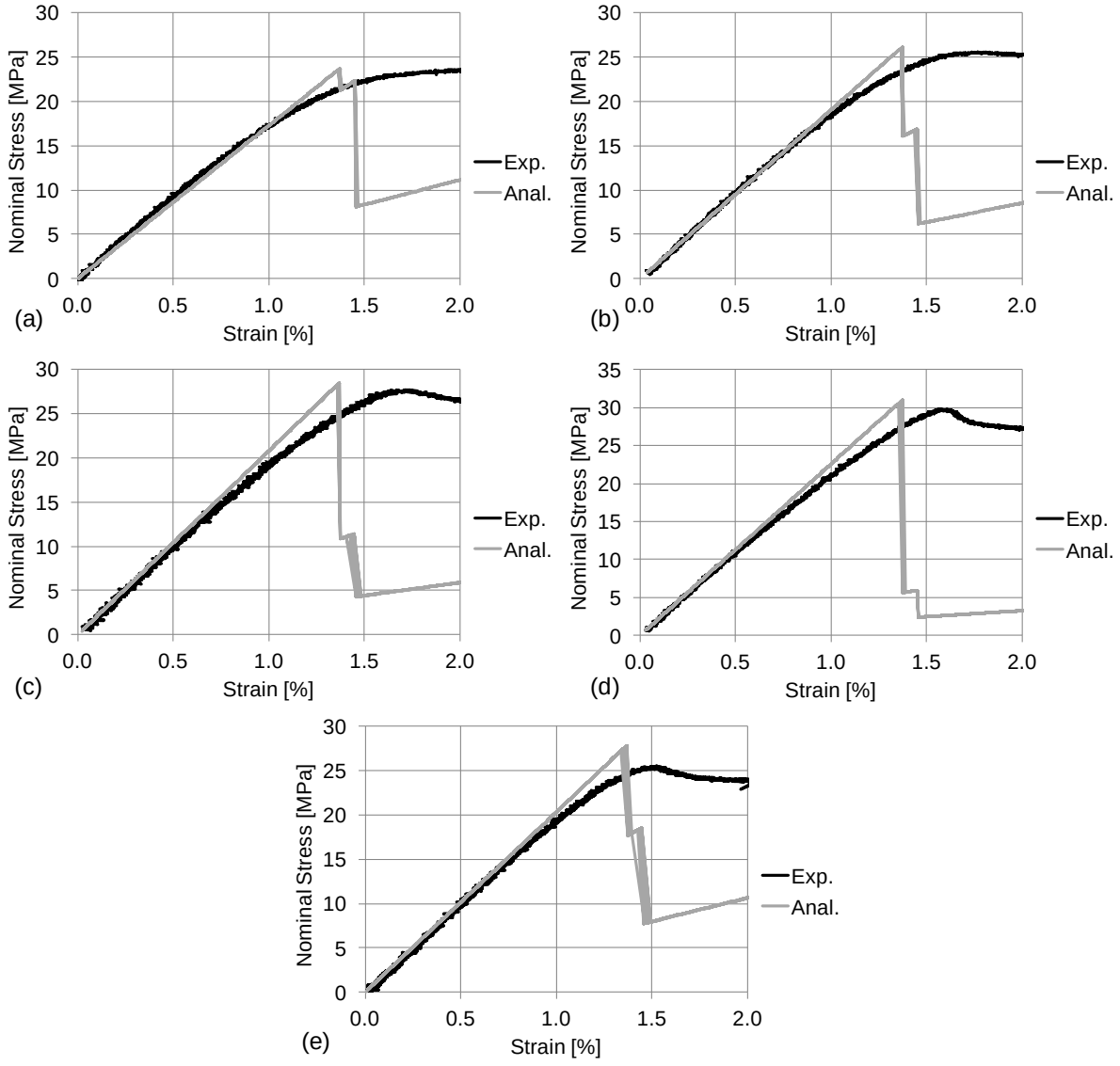

Fig.10 Comparison between analytically simulated and experimental stress-strain curves for different specimen types: (a) Type 1, (b) Type 2, (c) Type 3, (d) Type 4, (e) Type 5

The results of the analytical simulations of stress-strain curves are shown in Fig. 10, again with the reference to the five specimen types. The simulated curves are superimposed to the experimental curves: the comparison shows a very good agreement in the linear-elastic field.

The Young's moduli (E_a) have been computed, following the same procedure for the processing of the experimental data, according to *ASTM D638, 2010* Standard: the slopes of the linear parts of the curves have been estimated by linear fitting strategies. The computed elastic moduli are shown in the histogram of Fig. 11 (a): it compares the analytical yields to the experimental ones. The good agreement is, again, confirmed by the low percentage errors, never exceeding 6%.

The analysis of the diagrams reported in Fig. 10 shows that the response of the analytical model is not satisfactory in the plastic field, i.e. the model is unsuitable to predict the non-linear behaviour of the material. However, it can be argued that *FDM* products are usually loaded in the elastic field, even when huge deformations are required, thanks to their compliance properties (Lee, 2005). Moreover, the described model of the bead rupture event makes it possible to estimate the Ultimate Strength. The logical controls, as mentioned in the previous paragraph, automatically set the raster force to zero, when the *US* is overcome: this is the reason why the analytical curves experience abrupt decreases. The predicted strengths (US_a) have therefore been determined as the maximum values in the plotted curves. Analytical and experimental resistances are compared in the histogram in Fig. 11 (b). The results are again well consistent, with generally low percentage errors (up to 4%), except for the last specimen type (Type 5), where the error is about of 9%.

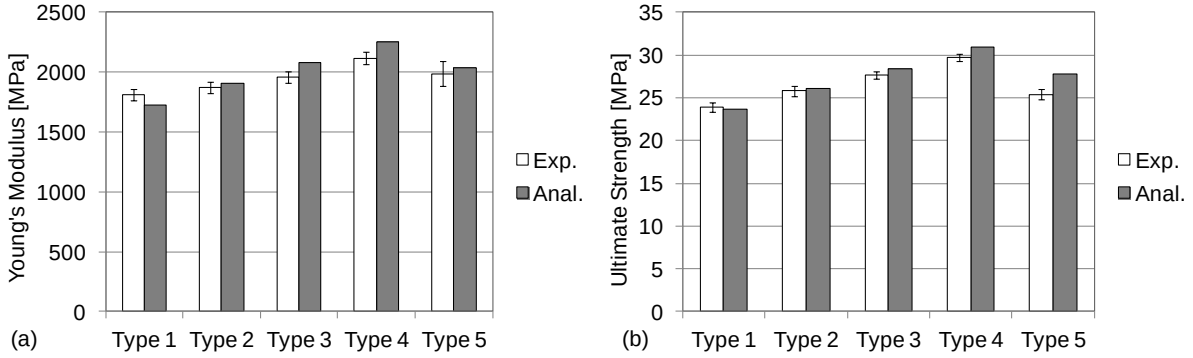

Fig.11 Comparison between the experimental data (Young's Modulus and Ultimate Strength) and the results of the analytical model

CONCLUSIONS

The present paper has dealt with the effect of contouring on the static strength and stiffness of *FDM* processed parts. The issue has been tackled both experimentally and analytically, with the development of a closed form predictive model. The main topics can be summarized in the following points.

- *FDM* is a rapid prototyping technique that makes it possible to build 3D parts at reduced costs in a reduced time. The low strength can be compensated by good compliance properties. The analysis of the state of the art has showed that the effect of contouring on the mechanical behaviour has never been studied and, furthermore, predictive models, which significantly relate the process parameters to the final properties, are actually missing.
- The study has been focused on *ABS-M30*, a widely used material for *FDM* processed parts. Specimens of five different types have been manufactured, taking two factors into account:

the building direction and the number of contours. Experimental tensile tests have been performed according to the *ASTM D638, 2010* Standard.

- The results have been processed for the determination of the Ultimate Strength and of the Young's modulus. Since a preliminary tentative of directly relating the number of contours to the mechanical retrieved characteristics produced inacceptable errors, it was decided to careful develop an analytical model, taking all the main process parameters into account and considering all the beads sharing the applied load.
- The analytical part has led to the development of stiffness models to be differently applied to the beads: contours placed longitudinally with respect to the load direction, and inclined beads having a fixed raster angle. The closed form algorithm that has been developed and presented is able to model the rupture event of every single bead and, consequently, to predict the failure of the whole part. Moreover, it can be easily implemented on a calc-sheet.
- The numerical results have been calibrated and validated by comparing them to the experimental outcomes. A really good agreement has been verified, as confirmed by very low errors (in the order of few percentage points) in the prediction of the Ultimate Strength, of the Young's module and of the stiffness of the tested samples.

REFERENCES

Ahn SH, Montero M, Odell D, Roundy S, Wright PK. Anisotropic material properties of fused deposition modelling ABS. Rapid Prototyping, 2002, 8(4), p. 248-257.

Anitha R, Arunachalam S, Radhakrishnan P. Critical parameters influencing the quality of prototypes in fused deposition modelling. Journal of Materials Processing Technology, 2001, 118, p. 385-388.

ASTM D638 – 10. Standard Test Method for Tensile Properties of Plastics. Annual Book of ASTM Standards, ASTM International, West Conshohocken, PA, USA, 2010.

Howell LL. Compliant Mechanism. Wiley, New York, 2001.

Lee BH, Abdullah J, Khan ZA. Optimization of rapid prototyping parameters for production of flexible ABS object. Journal of Materials Processing Technology, 2005, 169, p. 54-61.

Lee CS, Kim SG, Kim HJ, Ahn SH. Measurement of anisotropic compressive strength of rapid prototyping parts. Journal of Materials Processing Technology, 2007, 187-188, p. 627-630.

Olmi G. A New Loading-Constraining Device for Mechanical Testing with Misalignment Auto-Compensation. Experimental Techniques, 2011, 35(6), p. 61–70.

Sood AK, Ohdar RK, Mahapatra SS. Parametric appraisal of mechanical property of fused deposition modelling processed parts. Materials and Design, 2010, 31, p. 287-295.

Thrimurthulu K, Pandey PM, Reddy NV. Optimum part deposition orientation in fused deposition modelling. International Journal of Machine Tools & Manufacture, 2004, 44, p. 585-594.

Xu F, Loh HT, Wong YS. Considerations and selection of optimal orientation for different rapid prototyping systems. Rapid Prototyping Journal, 1999, 5(2), p. 54-60.